



## Article

# Regional Zenith Tropospheric Delay Modeling Based on Least Squares Support Vector Machine Using GNSS and ERA5 Data

Song Li <sup>1,2</sup>, Tianhe Xu <sup>2,\*</sup>, Nan Jiang <sup>2</sup>, Honglei Yang <sup>2</sup>, Shuaimin Wang <sup>2</sup> and Zhen Zhang <sup>2</sup>

<sup>1</sup> School of Geological and Surveying Engineering, Chang'an University, Xi'an 710054, China; 2018126024@chd.edu.cn

<sup>2</sup> Institute of Space Science, Shandong University, Weihai 264209, China; nanjiang@sdu.edu.cn (N.J.); hozzyee@mail.sdu.edu.cn (H.Y.); 201720576@mail.sdu.edu.cn (S.W.); 201916543@mail.sdu.edu.cn (Z.Z.)

\* Correspondence: thxu@sdu.edu.cn; Tel.: +86-631-5622731

**Abstract:** The meteorological reanalysis data has been widely applied to derive zenith tropospheric delay (*ZTD*) with a high spatial and temporal resolution. With the rapid development of artificial intelligence, machine learning also begins as a high-efficiency tool to be employed in modeling and predicting *ZTD*. In this paper, we develop three new regional *ZTD* models based on the least squares support vector machine (LSSVM), using both the International GNSS Service (*IGS*)-*ZTD* products and European Centre for Medium-Range Weather Forecasts Reanalysis 5 (*ERA5*) data over Europe throughout 2018. Among them, the *ERA5* data is extended to *ERA5S-ZTD* and *ERA5P-ZTD* as the background data by the model method and integral method, respectively. Depending on different background data, three schemes are designed to construct *ZTD* models based on the LSSVM algorithm, including the without background data, with the *ERA5S-ZTD*, and with the *ERA5P-ZTD*. To investigate the advantage and feasibility of the proposed *ZTD* models, we evaluate the accuracy of two background data and three schemes by segmental comparison with the *IGS-ZTD* of 85 *IGS* stations in Europe. The results show that the overall average Root Mean Square Errors (*RMSE*) value of all sites is 30.1 mm for the *ERA5S-ZTD*, and 10.7 mm for the *ERA5P-ZTD*. The overall average *RMSE* is 25.8 mm, 22.9 mm, and 9 mm for the three schemes, respectively. Moreover, the overall improvement rate is 19.1% and 1.6% for the *ZTD* model with *ERA5S-ZTD* and *ERA5P-ZTD*, respectively. In order to explore the reason of the lower improvement for the *ZTD* model with *ERA5P-ZTD*, the loop verification is performed by estimating the *ZTD* values of each available *IGS* station. In actuality, the monthly improvement rate of estimated *ZTD* is positive for most stations, and the biggest improvement rate can even reach about 40%. The negative rate mainly comes from specific stations, these stations are located on the edge of the region, near the coast, as well as the lower similarity between the individual verified station and training stations.

**Keywords:** zenith tropospheric delay (*ZTD*); least squares support vector machine (LSSVM); European Center for Medium-Range Weather Forecasts Reanalysis 5 (*ERA5*); Global Navigation Satellite System (GNSS)



**Citation:** Li, S.; Xu, T.; Jiang, N.; Yang, H.; Wang, S.; Zhang, Z. Regional Zenith Tropospheric Delay Modeling Based on Least Squares Support Vector Machine Using GNSS and ERA5 Data. *Remote Sens.* **2021**, *13*, 1004. <https://doi.org/10.3390/rs13051004>

Academic Editor: Roeland Van Malderen

Received: 6 January 2021

Accepted: 2 March 2021

Published: 6 March 2021

**Publisher's Note:** MDPI stays neutral with regard to jurisdictional claims in published maps and institutional affiliations.



**Copyright:** © 2021 by the authors. Licensee MDPI, Basel, Switzerland. This article is an open access article distributed under the terms and conditions of the Creative Commons Attribution (CC BY) license (<https://creativecommons.org/licenses/by/4.0/>).

## 1. Introduction

The troposphere constitutes most of the mass and water vapor of the entire atmosphere. The water vapor mainly concentrated in the troposphere below 10–12 km, which is an important meteorological factor causing climate change. With the rapid development of Global Navigation Satellite System (GNSS) technique, it has become an indispensable tool for monitoring water vapor variation [1,2]. When GNSS signals across the troposphere, these signals will slow down and bend because of the refraction of atmospheric molecules. The delay is usually described as the zenith tropospheric delay (*ZTD*) and the mapping function related to the elevation angle in the processing of GNSS data [3,4], and the water vapor variation can be retrieved and monitored by using high-precision *ZTD* values.

Therefore, the *ZTD* model with high spatiotemporal resolution has great significance to the research of global climate change monitoring.

The classic *ZTD* models were based on the measured meteorological parameters, such as the Saastamoinen model [5] and the Hopfield model [6]. However, these models were mostly employed for post-event calculation because the measured meteorological data were not easy to obtain in some places or in real time. Later, some researchers studied the temporal and spatial characteristics of meteorological parameters to propose meteorological models, such as the University of New Brunswick (UNB) series models [7], European Geostationary Navigation Overlay System (EGNOS) model [8], and the Global Pressure/Temperature (GPT) series model [9–11]. In these models, latitude and time information were used to express relevant meteorological elements [12]. The user could obtain the corresponding meteorological parameters at the research area by interpolation and fitting, and then the *ZTD* value could be estimated by combining these meteorological parameters with the classic *ZTD* models. This way had the advantage to satisfy the needs of GNSS real-time positioning. However, owing to the complexity of the wet components in *ZTD*, it was difficult to establish the *ZTD* model solely based on fixed physical formulas to satisfy high precision applications.

Interestingly, machine learning algorithms were emerged to solve the modeling and prediction problems of nonlinear variation at the end of the 20th century. Among them, some models were constructed based on the neural network (NN) algorithms to depict the complex atmospheric parameters and worked well [13–16]. The NN algorithms were also applied into the modeling of tropospheric path delay. Katsougiannopoulos and Pikridas [17] employed the NN algorithms to predict *ZTD* for various time spans of one, three, and six hours, and the results of their predictions possessed the agreements of 2–3 cm with *ZTD* derived from the network of continuously operating GNSS in Europe. In addition, the adaptive neuron fuzzy inference system (ANFIS) algorithm was proposed to establish the *ZTD* model based on a single GNSS station, where the input and output parameters of the model was the surface meteorological data and the estimated *ZTD* values at the GNSS station, respectively [18,19]. Moreover, Xiao, et al. [20] optimized the hyperparameters of the back propagation neural network (BPNN) algorithm to build the regional *ZTD* model in Japan, and this algorithm improved the fitting and prediction accuracy with Root Mean Square Errors (*RMSE*) of 7.8 mm and 8.5 mm, respectively. Furthermore, Zhang, et al. [21] derived an hourly high-accuracy *ZTD* model in west Antarctica by combining the BPNN algorithm, the long short-term memory (LSTM) network algorithm, as well as two blind source separation algorithms. Most existing *ZTD* models with the machine learning algorithms were based on the NN algorithms, but the NN algorithms may lead to a poor stability of performance and may be easy to fall into local minimum value.

The Least Squares Support Vector Machine (LSSVM) algorithm has a strong mathematical theory to support more stable *ZTD* modeling. Meanwhile, the European Centre for Medium-Range Weather Forecasts Reanalysis 5 (*ERA5*) data, as a fresh meteorological reanalysis data, starts to be provided in 2019. Afterward, the accuracy of the *ERA5* data began to be evaluated [22], and the *ERA5* data also started to calculate the *ZTD* values [23,24]. However, there are hardly researches on the *ERA5* data to build *ZTD* model based on machine learning algorithms, especially for the LSSVM algorithm. In this contribution, the LSSVM algorithm is introduced to develop three new regional *ZTD* models by combining both the International GNSS Service (*IGS*)-*ZTD* products and the *ERA5* data over Europe throughout 2018. Among them, the *ERA5* data is extended to *ERA5S-ZTD* and *ERA5P-ZTD* as the background by the model method and integral method, respectively. The background data acts as an external constrain of the *ZTD* modeling by LSSVM algorithm. Depending on different background data, three schemes are designed to construct *ZTD* models based on the LSSVM algorithm, including the without background data, using the *ERA5S-ZTD* as background data, and applying the *ERA5P-ZTD* as background data. Moreover, we also evaluate the accuracy of the derived two background data, as well as detailed analysis and discussion for the developed three *ZTD* models.

The structure of the article is as follows. Section 2.1 to Section 2.4 present the two mentioned data sources, the calculation method of two background data, the designed three ZTD models, and the strategy of accuracy evaluation, respectively. Sections 3.1 and 3.2 evaluate the accuracy of two background data and the three ZTD models, and Section 3.3 analyzes the improvement rate of the two ZTD models based on ERA5S-ZTD and ERA5P-ZTD in detail. In Section 4, we discuss the dependency of estimated ZTD on the station distribution, as well as on the output parameters. At last, the overview and outlook are given in Section 5.

## 2. Data and Methodology

### 2.1. Data Source

Since 1998, the IGS center has regularly provided the services of tropospheric error correction products. The troposphere products are offered in daily files by site for over 350 GNSS stations in the IGS network, which include five-minute estimates of ZTD and north and east troposphere gradient components, as well as the position of the IGS station. We can access to these products from IGS center (<ftp://igs.ensg.ign.fr/pub/igs/products/troposphere/>, accessed on 1 January 2021).

ERA5 data is the fifth-generation global meteorological parameter reanalysis data updated by the European Centre for Medium-Range Weather Forecasts (ECWMF) in January 2019. The ERA5 data is the grid data with a spatial resolution of  $0.25^\circ * 0.25^\circ$  and is provided with one-hour time resolution. It is divided into two types of data, namely the hourly data on single level and the hourly data on pressure levels, both of them can be taken from ECWMF center (<https://www.ecmwf.int/en/forecasts/datasets/reanalysis-datasets/era5>, accessed on 1 January 2021). The single-level products refer to the meteorological parameters on the surface of Earth. The pressure-level products divide the atmosphere into 37 pressure layers in vertical and provide meteorological parameters on the surface of each pressure layer, which enable ERA5 data to describe changes in meteorological parameters in more detail.

In both types of data, the IGS final product offer ZTD with a temporal resolution of 5 min, while these ZTD values have low spatial resolution owing to the uneven distribution of IGS stations all over the world. Interestingly, the ZTD values can reach a fixed spatial resolution of  $0.25^\circ * 0.25^\circ$  with hourly ERA5 data on a global scale. To unify the temporal resolution of the two types of data, we extract the hourly ZTD values from IGS products, namely IGS-ZTD in this contribution.

### 2.2. Two Background Data

By using the model method and the integral method, we derive the ZTD values at IGS stations as two background data based on the ERA5 data, namely ERA5S-ZTD and ERA5P-ZTD, respectively. Our specific calculation steps are as follows:

1. Obtaining original ERA5 data and the position of IGS station. In this study, the ERA5 hourly geopotential (m), 2-meter dewpoint temperature (K), 2-meter temperature (K), surface pressure (Pa) on single-level data, as well as the ERA5 hourly geopotential (m), temperature (K), and specific humidity (%) on 37 pressure-level data are utilized. The latitude, longitude and altitude of the IGS stations are extracted from the tropospheric products.
2. Getting the WGS84 ellipsoid height. Based on the EGM2008 [25], the ERA5 hourly geopotential of the single-level and the pressure-level products are corrected to ellipsoid height  $H_s$  and  $H_p$ , respectively.
3. Deriving meteorological parameters of the IGS stations using the single-level ERA5 data. According to the latitude and longitude of the IGS station, we detect the positions of the four nearest grid points of ERA5 data firstly. Then, the temperature  $T_s$ , 2-meter dewpoint  $T_{ds}$ , pressure  $P_s$  of the IGS stations at the height of  $H_s$  are derived through plane interpolation and fitting. Afterwards, these parameters are transformed from the height of  $H_s$  to the altitude  $H$  of the IGS stations. Among them, the altitude

difference  $dH$  between  $H_s$  and  $H$  are computed. The corresponding meteorological parameters of the IGS station,  $T$ ,  $T_d$  and  $P$  are derived by the following equations. At last, and the water vapor pressure  $e$  is calculated using  $T$  and  $T_d$ .

$$T = T_s - 6.5 \times dH \quad (1)$$

$$T_d = T_{ds} - 6.5 \times dH \quad (2)$$

$$P = P_s \times \left(1 - \frac{6.5}{T} \times dH\right)^{5.2559} \quad (3)$$

$$R_h = \frac{R_2 \times \exp\left(\frac{R_3 \times (T_d - 273.16)}{T_d - R_4}\right)}{R_2 \times \exp\left(\frac{R_3 \times (T - 273.16)}{T - R_4}\right)} \times 100\% \quad (4)$$

$$e = R_h \times \exp\left(-34.2465 + 0.213166 \times T - 0.000256908 \times T^2\right) \quad (5)$$

where,  $R_h$  represents the relative humidity, and the values of  $R_2 = 6.112$  hpa,  $R_3 = 17.502$  K, as well as  $R_4 = 32.19$  K.

- Calculating *ERA5S-ZTD* by the model method from  $T$ ,  $P$  and  $e$ . These meteorological parameters are substituted into the Saastamoinen model [5], and then *ERA5S-ZTD* values of the IGS stations are obtained using the following equations.

$$ERA5S - ZTD = 0.002277 \times \frac{[P + (\frac{1255}{T} + 0.05) \times e]}{1 - 0.0026 \cos(2\varphi) - 0.00028H} \quad (6)$$

where,  $\varphi$  denotes the latitude of the IGS stations.

- Interpolating meteorological parameters above the IGS stations by the pressure-level *ERA5* data. According to the relationship of  $H_P$  and  $H$ , the pressure-level data above the IGS stations are retained. Through the plane interpolation and fitting, the temperature  $T_P$  and specific humidity  $Q_P$  of the IGS stations at retained height of  $H_P$  are derived. The water vapor pressure  $e_P$  is obtained through  $Q_P$  and  $P_P$ .

$$e_P = \frac{Q_P \times P_P}{0.622} \quad (7)$$

where,  $P_P$  is the pressure value of each level.

- Calculating *ERA5P-ZTD* by the integral method. The *ERA5P-ZTD* values of the IGS stations are obtained by integrating as shown in the following equations [4].

$$N_S = K_1 \times \frac{P - e}{T} + K_2 \times \frac{e}{T} + K_3 \times \frac{e}{T^2} \quad (8)$$

$$N_P = K_1 \times \frac{P_P - e_P}{T_P} + K_2 \times \frac{e_P}{T_P} + K_3 \times \frac{e_P}{T_P^2} \quad (9)$$

$$N = \begin{bmatrix} N_P \\ N_S \end{bmatrix} \quad (10)$$

$$ERA5P - ZTD = 10^{-6} \int_H^{H_{top}} N dH \quad (11)$$

where,  $N_S$  refers to the atmospheric refractive index at the IGS stations,  $N_P$  represents the atmospheric refractive index above the IGS stations, and  $N$  contains the  $N_S$  and  $N_P$  in each IGS station.  $K_1$ ,  $K_2$  and  $K_3$  are the refractive index constants with the values of 77.604 K/hPa, 64.79 K/hPa and 377,600 K<sup>2</sup>/hPa, respectively.

### 2.3. Three Schemes Based on the LSSVM Algorithm

#### 2.3.1. LSSVM Algorithm

The training sets  $(x_{train\_i}, y_{train\_i})_{i=1,2,3...m}$  and testing sets  $(x_{test\_i}, y_{test\_i})_{i=1,2,3...n}$  are constructed using known data according to the network structure of different schemes,  $x$  and  $y$  represent the input and output vectors, respectively. The numbers of training sample and testing sample are described as  $m$  and  $n$ .

For a given training sample  $(x_{train\_i}, y_{train\_i})$ , the LSSVM algorithm constructs the special function, that is combined with the least-squares equation constraint conditions, to obtain the corresponding Lagrange function equation. The hyper-parameters of optimal model are obtained through the cross-validation method. The optimal solution conditions and the Radial Basis Function (RBF) kernel function matrix  $K$  are assembled to compose the LSSVM regression model. These above-mentioned processing is elucidated by the ensuing equations [26].

$$y_{train\_i} = \omega^T \times \phi(x_{train\_i}) + b + E \quad (12)$$

$$\min j(\omega, b, E) = \frac{1}{2} \omega^T \omega + C \frac{1}{2} E^T \quad (13)$$

$$L(\omega, b, E, \alpha) = j(\omega, b, E) - \sum_{i=1}^N \alpha_i \times \{y_{train\_i} [\omega^T \times \phi(x_{train\_i}) + b] + E_i - 1\} \quad (14)$$

$$y_{train\_i} = \sum_{i=1}^N \alpha_i \times K(x_{train\_i}, x_{train\_j}) + b \quad (15)$$

$$K(x_i, x_j) = \exp\left(\frac{-\|x_i - x_j\|^2}{2\sigma^2}\right) \quad (16)$$

where,  $\omega$  represents the weight vector,  $\phi$  denotes the mapping function,  $\alpha$  and  $b$  are the model parameters,  $E$  refers to the error vector of the model,  $C$  refers to the regularization constant, and  $\sigma$  explains the indicator of the kernel function, which is determined by the cross-validation optimization algorithm. In addition, Table 1 lists the initial parameters and optimization strategy settings of the LSSVM algorithms in this contribution.

**Table 1.** Initial parameters setting of the LSSVM algorithm.

| Parameter Name         | Value                 |
|------------------------|-----------------------|
| C                      | 10,000                |
| $\sigma^2$             | 2                     |
| type                   | 'function estimation' |
| kernel                 | 'RBF_kernel'          |
| preprocess             | 'preprocess'          |
| Method of optimization | 'grid search'         |
| Method of testing      | 'crossvalidatalssvm'  |

#### 2.3.2. Three Schemes

Based on the LSSVM algorithm, we design three schemes to establish the *ZTD* models according to different background data, namely Scheme 1, Scheme 2, and Scheme 3. The final *ZTD* estimations of three *ZTD* models are regarded as *EST-ZTD1*, *EST-ZTD2*, and *EST-ZTD3* respectively. It should be pointed that, the *ZTD* data is normalized to [0,1] when the *ZTD* data is taken as one of input parameters to directly participate in the *ZTD* modeling based on the LSSVM algorithm, in which the *ZTD* data includes the *IGS-ZTD*, the *ERA5S-ZTD*, as well as *ERA5P-ZTD*.

Scheme 1: The core of this scheme is employing the LSSVM algorithm to depict the functional relationship between the station position and the *ZTD* value, as shown in Figure 1. The input parameters are the longitude, latitude, altitude of the *IGS* stations, and the output elements are the estimated *IGS-ZTD* at the corresponding *IGS* stations. There is no background data involved in the *ZTD* model. This scheme is also employed in most *ZTD* models based on machine learning algorithms. When we verify the trained

model by testing stations, the *EST-ZTD1* at the test station is the output *ZTD* value of this model.

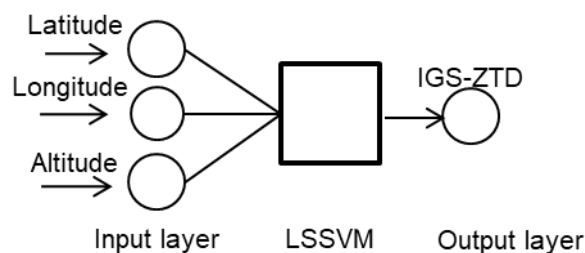


Figure 1. Network structure of Schemes 1.

Scheme 2: We introduce the *ERA5S-ZTD* as background data in the *ZTD* model. The core of this scheme is to estimate the deviation of *ERA5S-ZTD* and *IGS-ZTD* by the LSSVM algorithm, the network structure is shown in Figure 2. In this scheme, the longitude, latitude, altitude, and the *ERA5S-ZTD* of the *IGS* station constitute the input vector. The corresponding output parameter is the deviation  $D-ZTD_{ERA5S}$  depicted through the following equation. In the last, the *EST-ZTD2* of the test station is the summation of the estimated  $D-ZTD_{ERA5S}$  and the corresponding *ERA5S-ZTD*.

$$D - ZTD_{ERA5S} = IGS - ZTD - ERA5S - ZTD \tag{17}$$

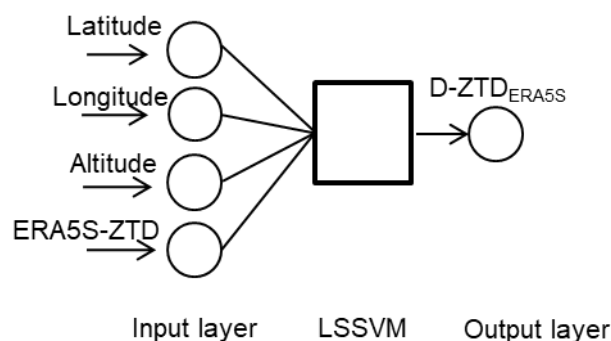


Figure 2. Network structure of Scheme 2.

Scheme 3: Similar as Scheme 2, the *ERA5P-ZTD* replaces the *ERA5S-ZTD* as the background data in Scheme 3, as shown in the following equation and in Figure 3.

$$D - ZTD_{ERA5P} = IGS - ZTD - ERA5P - ZTD \tag{18}$$

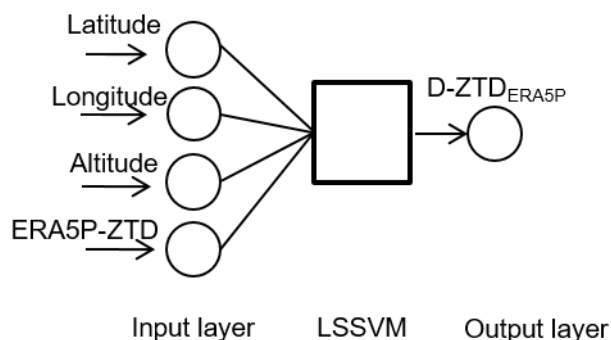


Figure 3. Network structure of Scheme 3.

#### 2.4. Accuracy Evaluation

The *IGS-ZTD* is adopted as the true value because it can reach a high precision of 4 mm. Due to the poor data integrity of some stations in a long time period, we divide the year into 12 months to ensure a sufficient number of samples in the research stage. The monthly bias and the root mean square error (*RMSE*) of each experimental *IGS* station are calculated by the following equations. The verifications of three *ZTD* models are evaluated by the average monthly bias and average *RMSE* of all testing stations in each month. In addition, piece-wise evaluations of two different background data are performed at each session. The evaluation indexes are the same as that of the *ZTD* model.

$$\text{Monthly\_bias} = \frac{1}{N} \sum_{i=1}^N (\text{EST-ZTD}_i - \text{IGS-ZTD}_i) \quad (19)$$

$$\text{RMSE} = \sqrt{\frac{1}{N} \sum_{i=1}^N (\text{EST-ZTD}_i - \text{IGS-ZTD}_i)^2} \quad (20)$$

where,  $N$  is the monthly number of *EST-ZTD* values for each available station.

### 3. Results and Analysis

The *ERA5* hourly data of the European region (32° N–72° N, 15° W–40° E) in 2018 are extended to the *ERA5S-ZTD* and the *ERA5P-ZTD* at the positions of 85 *IGS* stations. More than 50 *IGS* stations are available per month, and all of them are employed to investigate the consistency of the extended *ERA5S-ZTD* and *ERA5P-ZTD* with *IGS-ZTD*. Moreover, 10 available *IGS* stations are selected in each month to verify the accuracy of our three *ZTD* models, where these models are built by the remaining more than 40 *IGS* stations derived from the three schemes. Figure 4 displays the distribution of experimental *IGS* stations in January 2018.

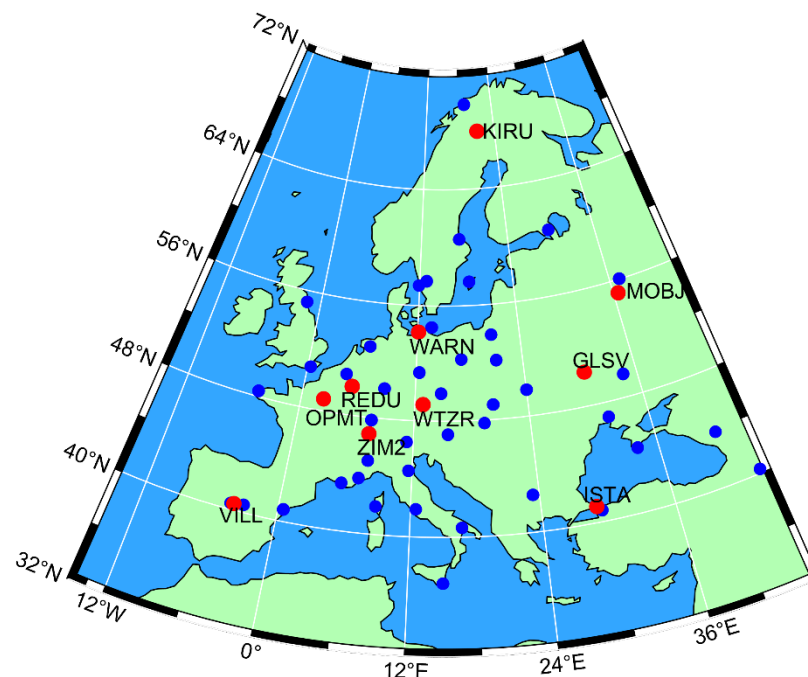


**Figure 4.** Distribution of experimental *IGS* stations in January 2018. Blue spots represent the training sites, and 10 testing sites are shown by red points.

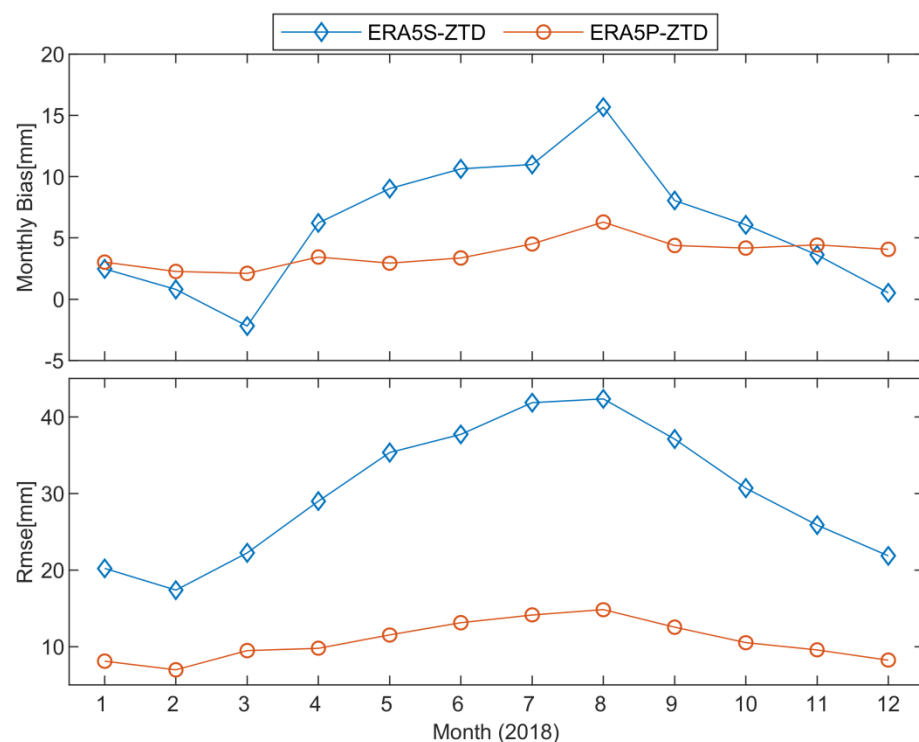
#### 3.1. Accuracy of Two Background *ZTD*

Table 2 shows the monthly bias and *RMSE* of the *ERA5S-ZTD* and *ERA5P-ZTD* by comparison with the *IGS-ZTD* at all available stations. For the *ERA5S-ZTD*, the average bias values are in the range of  $-2.2$ – $15.7$  mm, with the corresponding average *RMSE*

values of 17.4–42.3 mm. Generally, the higher the absolute value of the monthly bias has, the bigger the average *RMSE* value is. The largest average monthly bias is 15.7 mm with the maximum and minimum values of 68.4 mm and  $-26.6$  mm in August 2018, respectively. Subsequently, the maximum and minimum values of the corresponding *RMSE* are 18.8 mm and 83.7 mm. For the *ERA5P-ZTD*, all of the average monthly biases are positive values with the range of 2.1–6.3 mm, and the corresponding average *RMSE* values are in the range of 7–14.8 mm. Meanwhile, only several *RMSE* values exceed 20 mm with the maximum *RMSE* value of 27.1 mm in June 2018.

**Table 2.** Monthly bias and *RMSE* of the *ERA5S-ZTD* and *ERA5P-ZTD* by comparison with the *IGS-ZTD* at all available stations. Values in brackets refer to the monthly minimal and maximal value for all available stations. Unit is millimeter.

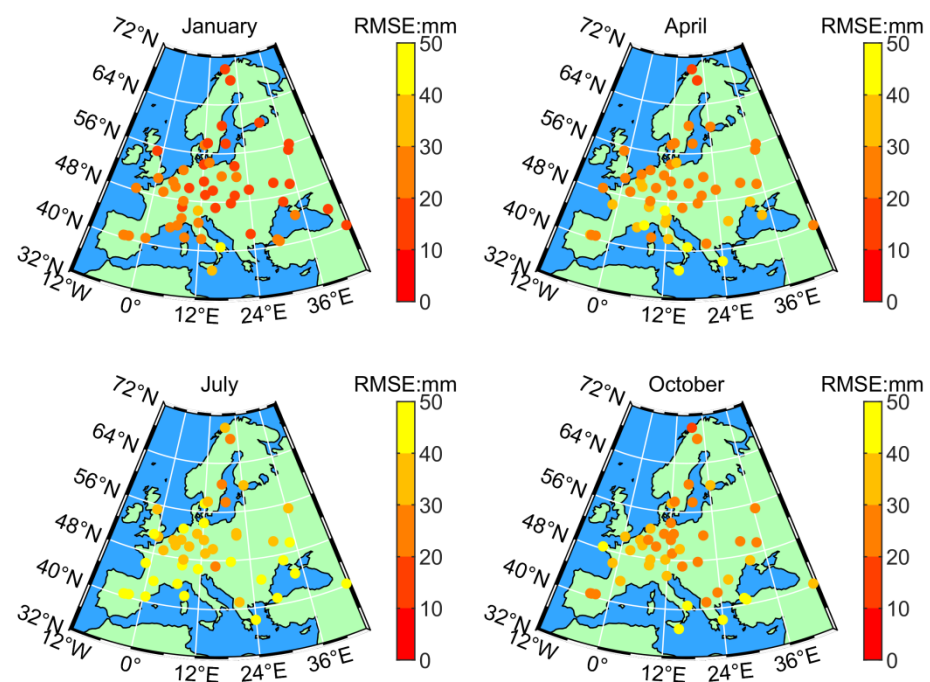
|           | <i>ERA5S-ZTD</i>  |                  | <i>ERA5P-ZTD</i> |                  |
|-----------|-------------------|------------------|------------------|------------------|
|           | Monthly Bias      | <i>RMSE</i>      | Monthly Bias     | <i>RMSE</i>      |
| January   | 2.5 [−29.6,32.9]  | 20.2 [10.4,41.1] | 3.0 [−9.6,12.8]  | 8.1 [4.6,17.1]   |
| February  | 0.8 [−16.3,25.6]  | 17.4 [8.4,30.6]  | 2.3 [−14.7,11.8] | 7.0 [3.4,14.0]   |
| March     | −2.2 [−26.7,15.0] | 22.2 [7.2,36.5]  | 2.1 [−12.2,17.8] | 9.5 [4.9,19.7]   |
| April     | 6.2 [−37.0,42.3]  | 29.0 [10.6,54.7] | 3.5 [−10.4,21.8] | 9.8 [4.7,23.2]   |
| May       | 9.0 [−53.7,40.4]  | 35.3 [23.0,60.2] | 2.9 [−14.1,19.5] | 11.5 [6.7,22.0]  |
| June      | 10.6 [−13.9,39.1] | 37.7 [15.1,68.1] | 3.4 [−11.9,24.0] | 13.1 [5.9,27.1]  |
| July      | 11.0 [−7.5,62.0]  | 41.8 [26.0,81.3] | 4.5 [−12.9,18.7] | 14.1 [10.0,23.9] |
| August    | 15.7 [−26.6,68.4] | 42.3 [18.8,83.7] | 6.3 [−12.9,21.8] | 14.8 [6.9,26.1]  |
| September | 8.1 [−49.1,52.7]  | 37.1 [7.3,66.4]  | 4.4 [−9.1,21.7]  | 12.5 [7.8,24.3]  |
| October   | 6.1 [−23.3,35.6]  | 30.7 [16.9,46.6] | 4.2 [−8.3,24.3]  | 10.5 [6.2,25.8]  |
| November  | 3.6 [−24.0,37.3]  | 25.9 [16.5,46.7] | 4.4 [−10.8,12.5] | 9.6 [5.6,17.0]   |
| December  | 0.5 [−17.7,20.1]  | 21.9 [14.4,33.3] | 4.1 [−2.9,21.3]  | 8.2 [4.2,22.3]   |
| Mean      | 6.0               | 30.1             | 3.8              | 10.7             |



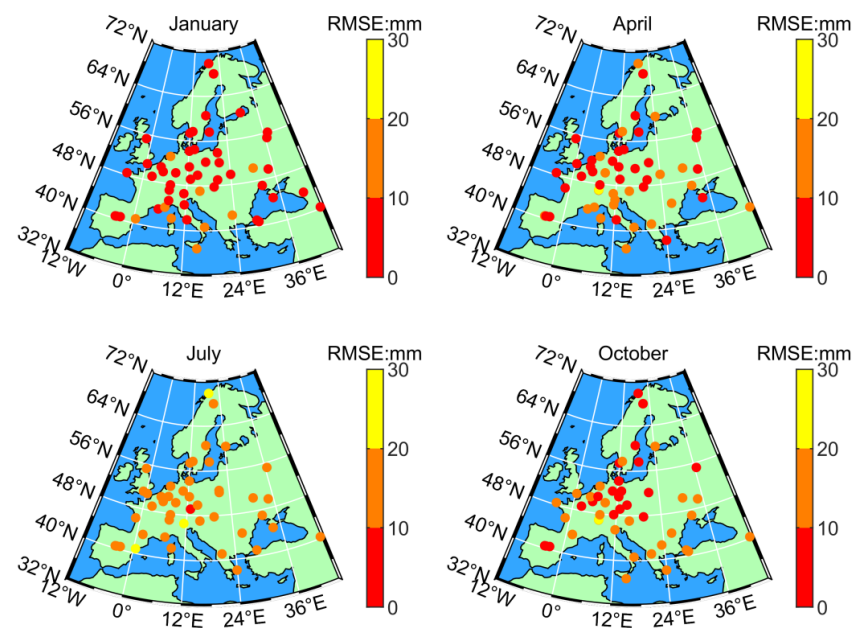
**Figure 5.** Average monthly bias and average *RMSE* of *ERA5S-ZTD* and *ERA5P-ZTD* in 2018.

Figure 5 demonstrates the average monthly bias and the average *RMSE* values of two background *ZTD*. The average monthly bias of *ERA5S-ZTD* is larger than that of *ERA5P-ZTD* from March to October 2018, with the more obvious variation. The average *RMSE* series of both *ERA5S-ZTD* and *ERA5P-ZTD* appear the same trend of rising firstly and then falling over time, and the average *RMSE* of *ERA5S-ZTD* is greater than that of *ERA5P-ZTD* in each month, especially from May to October. These results imply that *ERA5S-ZTD* has a larger systematic bias with the *IGS-ZTD* than the *ERA5P-ZTD*, and the consistency between *ERA5P-ZTD* and *IGS-ZTD* are better than that of between *ERA5S-ZTD* and *IGS-ZTD*. The reasons are caused by both the difference of the grid data and the processing methods. On one hand, the extended *ERA5S-ZTD* only uses hourly *ERA5* data on the single-level data, while the hourly data on 37 pressure levels are employed in the extended *ERA5P-ZTD*. On the other hand, the *ERA5S-ZTD* is obtained by substituting the meteorological parameters into the fixed model, which may have certain system errors, while the *ERA5P-ZTD* is computed by integrating all the refractive across the path of the GNSS signals.

Figures 6 and 7 show the *RMSE* values of all available *IGS* stations derived from the *ERA5S-ZTD* and *ERA5P-ZTD* in January, April, July, and October of 2018, respectively. This corresponds to winter, spring, summer, and autumn in the northern hemisphere. The *RMSE* values of each station in January are relatively small for both the *ERA5S-ZTD* and *ERA5P-ZTD*, and the highest *RMSE* appears for these stations in July. This indicates that the situation is a common feature of the whole selected region. The value for tropospheric delay changes with different seasons and latitudes because there are complex meteorological phenomena in the troposphere [27]. In different seasons, the diverse moisture content brings the seasonal variation of the *ZTD* values. When the summer is coming, the change of the moisture content can get complex and dramatic in a smaller area, while the ability of minor change capturing is limited for the *ERA5* grid data. Moreover, the lower *RMSE* values are always distributed in high latitudes and inland areas, as well as the higher *RMSE* values mostly appear in low latitudes and coastal regions. It implies that the high heat and active monsoon activities lead to the large and complex *ZTD* value in low latitudes and coastal areas. The *ERA5* data does not indicate this variety of *ZTD* values perfectly, which brings about this spatial characteristic of *RMSE* values.



**Figure 6.** *RMSE* values of *ERA5S-ZTD* at all available *IGS* stations in January, April, July, and October of 2018. These *RMSE* values of *ERA5S-ZTD* are concentrating in the range of 25–50 mm.



**Figure 7.** RMSE values of ERA5P-ZTD at all available IGS stations in January, April, July, and October of 2018. These RMSE values of ERA5P-ZTD are always less than 20 mm.

### 3.2. Accuracy of Three Schemes

We verify the consistency of our three ZTD models by comparison the estimated ZTD values with IGS-ZTD. Table 3 gives their monthly bias and RMSE values of 10 verification stations. The overall average monthly bias is 1.1 mm, 0.3 mm, and  $-1.6$  mm for Scheme 1, 2, and 3, respectively. The mean value of the average RMSE of 12 months is 25.8 mm, 22.9 mm, and 9.0 mm for Schemes 1, 2, and 3, respectively. Among them, the average monthly bias of 10 verification stations of Scheme 1 is in the range of  $-3.5$ – $9.3$  mm, the corresponding average RMSE values are within 16.9–33.9 mm. The maximum monthly bias of 36.7 mm appears on the individual verification station in August, as well as the maximum RMSE of 52.3 mm. For Scheme 2, the average monthly bias is relatively small with the range of  $-2.4$ – $4.4$  mm in 12 months and the average RMSE is concentrated in the 15.3–30.4 mm. One of 10 verification stations has the maximum monthly bias of 32.4 mm and maximum RMSE value of 54.2 mm in September. In addition, all of the average monthly biases of Scheme 3 are negative values from  $-0.7$  mm to  $-3.5$  mm with the corresponding average RMSE values from 6.1 mm to 12.6 mm.

**Table 3.** Monthly bias and RMSE values of 10 verification stations. Values in brackets refer to the monthly minimal and maximal value for 10 verifying stations. Unit is millimeter.

|           | EST-ZTD1                |                  | EST-ZTD2                |                  | EST-ZTD3              |                  |
|-----------|-------------------------|------------------|-------------------------|------------------|-----------------------|------------------|
|           | Monthly Bias            | RMSE             | Monthly Bias            | RMSE             | Monthly Bias          | RMSE             |
| January   | $-2.7$ [ $-17.7,8.9$ ]  | 21.0 [12.1,33.0] | 0.2 [ $-10.0,11.1$ ]    | 15.9 [9.4,21.5]  | $-0.7$ [ $-6.8,5.9$ ] | 6.6 [4.4,9.4]    |
| February  | $-2.0$ [ $-20.6,4.0$ ]  | 16.9 [7.9,35.1]  | $-1.3$ [ $-13.6,8.3$ ]  | 15.3 [9.5,27.8]  | $-0.9$ [ $-6.4,5.2$ ] | 6.1 [4.0,8.1]    |
| March     | $-1.9$ [ $-12.3,13.3$ ] | 18.5 [9.5,29.1]  | 0.3 [ $-6.9,9.1$ ]      | 17 [8.0,27.0]    | $-0.9$ [ $-6.5,5.1$ ] | 7.4 [5.2,9.6]    |
| April     | 5.2 [ $-4.7,26.6$ ]     | 21.9 [9.7,36.6]  | 2.2 [ $-5.7,21.0$ ]     | 19.7 [8.6,33.1]  | $-2.1$ [ $-8.5,5.5$ ] | 8.3 [5.2,11.4]   |
| May       | 2.9 [ $-10.9,17.1$ ]    | 29.9 [18.5,48.7] | $-1.1$ [ $-17.5,20.7$ ] | 25.7 [17,35]     | $-1.3$ [ $-7.5,5.9$ ] | 10 [8.5,12.2]    |
| June      | 5.6 [ $-9.1,27.5$ ]     | 33.9 [20,48.2]   | 1.5 [ $-8,17.1$ ]       | 28.2 [18,46]     | $-1.8$ [ $-6.6,2.3$ ] | 11.1 [8.5,13.2]  |
| July      | $-2.2$ [ $-15.8,15.6$ ] | 32.8 [22.2,49.1] | $-2.4$ [ $-16.9,9.9$ ]  | 30.4 [18.2,43.7] | $-2.3$ [ $-7.9,2.6$ ] | 12.6 [10.9,14.0] |
| August    | 9.3 [ $-11.2,36.7$ ]    | 33 [22.8,52.3]   | 2.3 [ $-9.7,28.5$ ]     | 30 [17.4,44.2]   | $-1.9$ [ $-7.6,2.5$ ] | 11.8 [7.3,14.9]  |
| September | 2.8 [ $-14.4,13.6$ ]    | 29.2 [15.7,48.9] | 4.4 [ $-8.6,32.4$ ]     | 28.7 [13.4,54.2] | $-1.3$ [ $-6.2,6.4$ ] | 10.2 [6.7,13.1]  |
| October   | 0 [ $-11.0,3.9$ ]       | 26.8 [14.0,40.5] | 0.1 [ $-12.6,15.3$ ]    | 23.9 [15.2,35.5] | $-1.4$ [ $-7.2,6.3$ ] | 8.7 [6.5,10.7]   |
| November  | $-0.1$ [ $-9.8,7.9$ ]   | 23.4 [10.0,40.4] | $-1$ [ $-9.2,16.8$ ]    | 21.5 [13.4,42.8] | $-1.4$ [ $-6.4,7.0$ ] | 7.7 [5.8,10.3]   |
| December  | $-3.5$ [ $-21.3,15.3$ ] | 22.1 [9.7,31.3]  | $-1.7$ [ $-9.5,7.3$ ]   | 18.3 [11.7,23.8] | $-3.5$ [ $-7.9,0.5$ ] | 7.2 [5.1,9.1]    |
| Mean      | 1.1                     | 25.8             | 0.3                     | 22.9             | $-1.6$                | 9.0              |

Figure 8 visualizes the average monthly bias and average *RMSE* per month. All of the average monthly biases of Scheme 1 and Scheme 2 go up and down around zero in 12 months; that of Scheme 3 is close to zero. These results illustrate that the overall systematic errors are small for all three *ZTD* models based on the *LSSVM* algorithm. Interestingly, a near overlap emerges owing to the more negative monthly bias values of three schemes in July 2018. Meanwhile, a temporal feature emerges for the average *RMSE* values of three *ZTD* models, where the *RMSE* values grow in size with the coming of summer. It reflects a common problem that the accumulation of water vapor and the irregular changes of cyclones in summer lead to more difficulty in modeling *ZTD*. Moreover, the average *RMSE* values of Scheme 3 and Scheme 2 are smaller than that of Scheme 1, and the value of Scheme 3 is the smallest in each month. It indicates that the two models with extended *ERA5* data as background data have a significant advantage compared to the model without background data, and the accuracy of the model based on *ERA5P-ZTD* is better because the higher consistency occurs between the *ERA5P-ZTD* and *IGS-ZTD*.

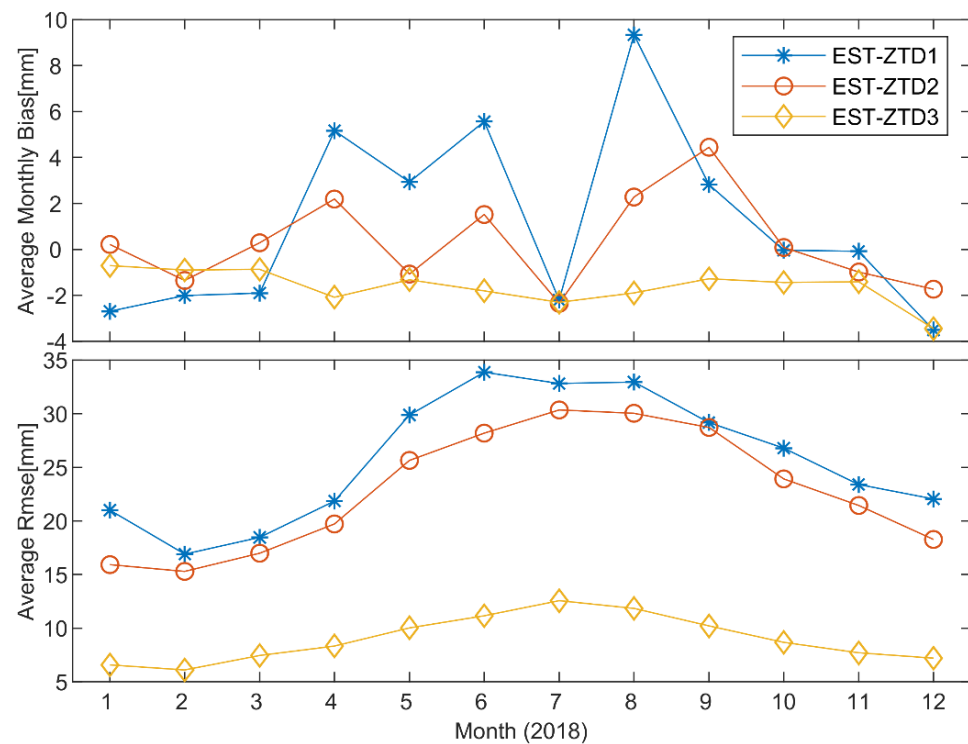


**Figure 8.** Average monthly bias and average *RMSE* of estimated *ZTD* values at 10 verifying *IGS* stations based on the three schemes.

### 3.3. Improvement Rate of the Two *ZTD* Models Based on *ERA5S-ZTD* and *ERA5P-ZTD*

To analyze the advantage of the two *ZTD* models of Scheme 2 and Scheme 3, we compare the *RMSE* values of the 10 verification stations derived from the two *ZTD* models with *ERA5S-ZTD* and *ERA5P-ZTD*, and their respective improvement rates are calculated according to the following two equations.

$$\text{Improvement\_Scheme2} = \frac{\text{RMSE}_{\text{ERA5S-ZTD}} - \text{RMSE}_{\text{EST-ZTD2}}}{\text{RMSE}_{\text{ERA5S-ZTD}}} \times 100\% \quad (21)$$

$$\text{Improvement\_Scheme3} = \frac{\text{RMSE}_{\text{ERA5P-ZTD}} - \text{RMSE}_{\text{EST-ZTD3}}}{\text{RMSE}_{\text{ERA5P-ZTD}}} \times 100\% \quad (22)$$

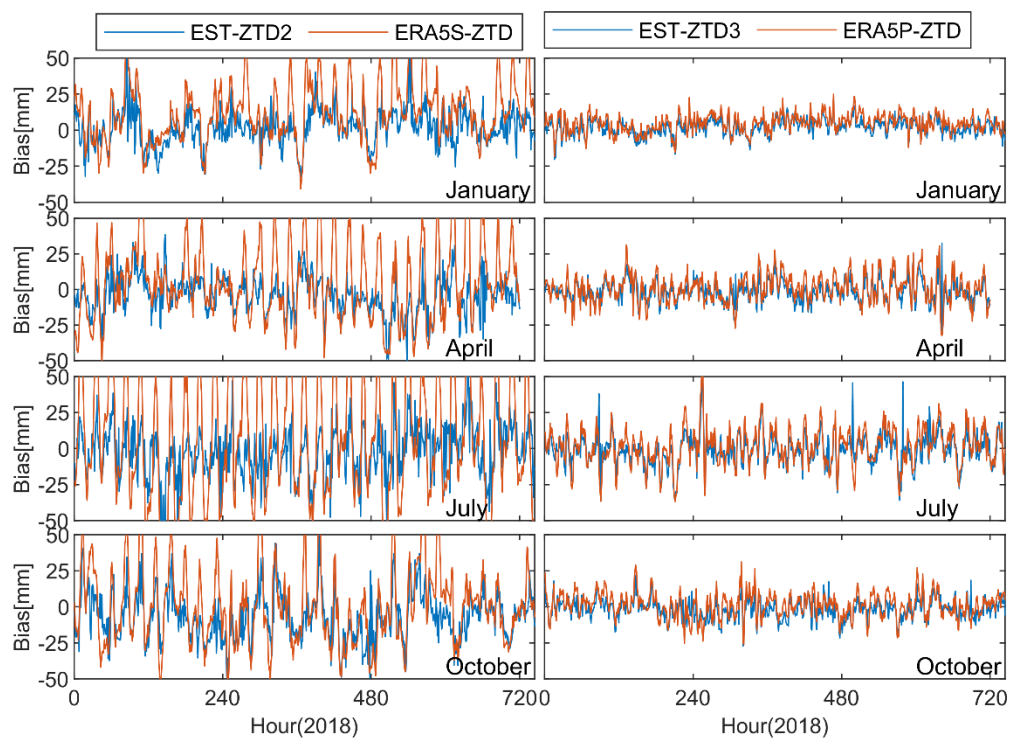
where, the  $RMSE_{ERA5S-ZTD}$  and  $RMSE_{ERA5P-ZTD}$  refer to the  $RMSE$  value of the  $ERA5S-ZTD$  and  $ERA5P-ZTD$  in each verified station, respectively. The  $RMSE_{EST-ZTD2}$  and  $RMSE_{EST-ZTD3}$  represent the  $RMSE$  values of Scheme 2 and Scheme 3 at 10 verification stations.

Table 4 lists the statistical result of the improvement rate based on 10 verification stations. For Scheme 2, the overall average improvement rate reaches 19.1%, with the monthly average improvement rate of from 12.7% to 26.3%. In these months, the optimal improvement rate is up to 61.3% at an individual station in July, as well as the worst rate of  $-64.7\%$  in June. For Scheme 3, only 1.6% overall average improvement rate is achieved, and most of the monthly average improvement rates are close to zero. During those 12 months, the best monthly average improvement rate is 17.5% with the maximum improvement of 42.5% at one of 10 verification stations in March, and the worst rate is  $-12.5\%$  with the rate of  $-86.1\%$  at an individual station in December. By comprehensively comparing the improvement rate of Scheme 2 and Scheme 3, it clearly stands out that the LSSVM algorithm has the excellent performance of compensating the errors derived from  $ERA5S-ZTD$ , while the situation is not obvious for the  $ERA5P-ZTD$ . Even so, the improvement rate of several stations can also exceed 17% in all 12 months for Scheme 3.

**Table 4.** Improvement rate of Schemes 2 and 3. Values in brackets refer to the monthly minimal and maximal improvement rate for 10 verifying stations. Unit is percent.

|           | Improvement-Scheme 2 | Improvement-Scheme 3 |
|-----------|----------------------|----------------------|
| January   | 18.8 [−0.1,48.8]     | 7.4 [−31.4,37.3]     |
| February  | 12.7 [−19.9,36.4]    | −0.2 [−35.2,35.1]    |
| March     | 20.7 [−10.0,43.3]    | 17.5 [−11.2,42.5]    |
| April     | 26.3 [2.5,50.7]      | −0.9 [−44.8,22.5]    |
| May       | 16.8 [−50.0,48.1]    | −2.2 [−32.3,19.0]    |
| June      | 16.4 [−64.7,45.5]    | −0.2 [−44.1,22.3]    |
| July      | 18.2 [−28.4,61.3]    | −1.8 [−19.6,17.7]    |
| August    | 23.9 [−10.8,46.3]    | 0.6 [−29.4,25.1]     |
| September | 23.4 [−1.4,46.2]     | 5.3 [−19.6,23.4]     |
| October   | 20.6 [−33.8,46.2]    | 0.4 [−32.3,28.9]     |
| November  | 17.8 [−3.3,45.3]     | 5.5 [−21.6,38.6]     |
| Dec       | 13.4 [−20.4,49.8]    | −12.5 [−86.1,33.8]   |
| Mean      | 19.1                 | 1.6                  |

As a typical, Figure 9 and Table 5 display the result of GLSV site in January, April, July, and October of 2018, where the GLSV site is one of the 10 verification stations. Among them, as shown in Figure 9 that significant periodic error signals exist in the bias time series of  $ERA5S-ZTD$  and have significantly improved after modeling with  $ERA5S-ZTD$  based on the LSSVM algorithm, especially in summer. For the bias time series of  $ERA5P-ZTD$ , the periodic error signals have a small fluctuation amplitude compared with  $ERA5S-ZTD$ , especially for the results in winter. In addition, the improvement effects from Scheme 3 are not better than that of Scheme 2. As can be seen from the monthly bias in Table 5,  $EST-ZTD2$  model has better correction effect for the obvious systematic errors in  $ERA5S-ZTD$  model compared with the improvement of  $EST-ZTD3$  relative to  $ERA5P-ZTD$ . Overall, the LSSVM algorithm has better performance in correcting periodic bias of the  $ERA5S-ZTD$ , and the extended  $ERA5P-ZTD$  by the integral method has good accuracy property, which constrains the improvement capability of the LSSVM algorithm.



**Figure 9.** Bias time series of *ZTD* estimations at the GLSV site in January, April, July, and October of 2018. The four subgraphs on the left refer to the bias time series from *ERA5S-ZTD* and Scheme 2, and four subgraphs on the right for the *ERA5P-ZTD* and Scheme 3.

**Table 5.** Monthly bias and *RMSE* of *ZTD* estimations from *ERA5S-ZTD*, *EST-ZTD2*, *ERA5P-ZTD* and *EST-ZTD3* model at the GLSV site in January, April, July, and October of 2018. Unit is millimeters.

|         | <i>ERA5S-ZTD</i> |             | <i>EST-ZTD2</i> |             | <i>ERA5P-ZTD</i> |             | <i>EST-ZTD3</i> |             |
|---------|------------------|-------------|-----------------|-------------|------------------|-------------|-----------------|-------------|
|         | Monthly Bias     | <i>RMSE</i> | Monthly Bias    | <i>RMSE</i> | Monthly Bias     | <i>RMSE</i> | Monthly Bias    | <i>RMSE</i> |
| January | −12.7            | 24.3        | 1.7             | 12.4        | −4.7             | 7.8         | 2.1             | 5.8         |
| April   | −5.5             | 28.8        | −4.4            | 14.2        | −0.7             | 9.8         | −1.4            | 7.7         |
| July    | −10.1            | 47.0        | −2.2            | 18.2        | −1.3             | 13.0        | −0.8            | 10.9        |
| October | −0.7             | 27.4        | −6.8            | 18.2        | −1.1             | 8.6         | −1.7            | 7.2         |

#### 4. Discussion

To further investigate the feasibility and availability of the *ZTD* model of Scheme 3, we perform loop verification on each of the all available *IGS* stations per month. In each month, each of the available *IGS* stations is as a testing station in turn to estimate *ZTD* values, and all remaining available *IGS* stations are used to train the *ZTD* model based on the *LSSVM* algorithm. Afterward, the *RMSE* values of these estimated *ZTD* values are evaluated by comparison with *IGS-ZTD* according to Equation (20), as well as the calculated improvement rate according to Equation (22). We calculate the percentage of all available *IGS* stations per month by dividing them into the accuracy-improved stations and the accuracy-reduced stations, as well as the overall average improvement rate of their *RMSE* values. Among them, the percentage of stations with accuracy-reduced stations can be subtracted by the percentage of accuracy-improved stations from 100%. As shown in Figure 10, the percentage of the accuracy-improved stations exceeds 50%, while the overall average improvement rate of *RMSE* values is less than 10% per month, with the exception of March 2018.

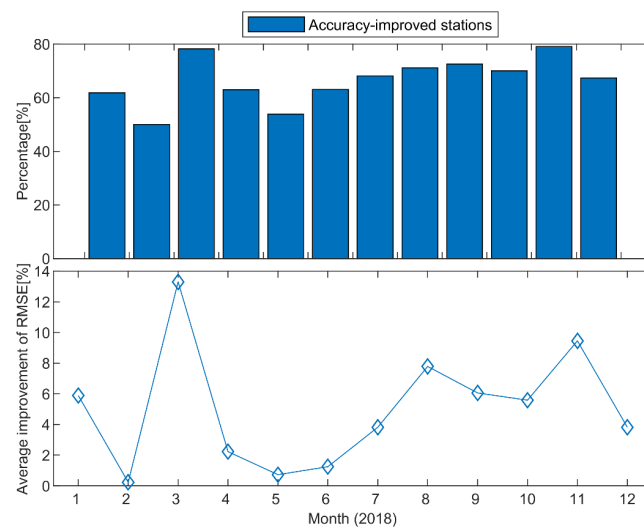


**Figure 10.** Statistical improvements of Scheme 3 at all stations. The up sub-figure depicts the proportion of accuracy-improved stations. The average improvement of *RMSE* at all stations is shown in the down subfigure.

#### 4.1. Dependency of the Estimated *ZTD* on the Station Distribution

Figure 11 unfolds the improvement rate of each available *IGS* station in January, April, July, and October of 2018. The most red and yellow spots with the improvement rate in the range of 0–40% are mainly located in the central region of Europe, where the available *IGS* stations evenly are distributed and compact. This allows that the information of input and output parameters can be comprehensively captured with precision in these areas. The mainly cyan and blue spots with the rate of −40%–0 are located in the edge of the station network or near the coast, and few stations adjacent to them. Therefore, no enough samples can be trained by using the *LSSVM* algorithm, and the stations located in the coastal area suffer from more drastic climate variability. Specially, several cyan and blue spots are surrounded by a dense network of stations in the central region, such as the *WTZR* site. It implies that good station distribution is not the unique requirement for the improvement of the estimated *ZTD*. Therefore, we make a further discussion for the dependency of estimated *ZTD* on the output parameters  $D\text{-}ZTD_{ERA5P}$  in the next section.

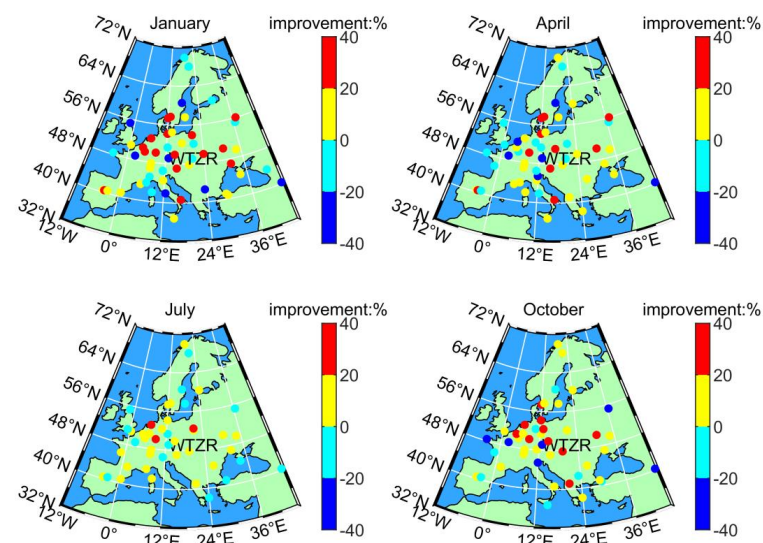


**Figure 11.** Distribution of improvement rate of all available stations from Scheme 3 in January, April, July, and October of 2018. Red spots refer to the improvement rate of the available *IGS* stations in the range of 0–20%, 20%–40% for yellow spots, −20%–0 for cyan spots, and −40%–−20% for blue spots.

#### 4.2. Dependency of the Estimated ZTD on the Output Parameter $D-ZTD_{ERA5P}$

According to the following formula, we calculate the cosine value of the monthly  $D-ZTD_{ERA5P}$  time series between the vector of the individual verified station and each of the training station [28].

$$\cos\left(D - ZTD_{ERA5P}^{train_i}, D - ZTD_{ERA5P}^{test}\right) = \frac{D - ZTD_{ERA5P}^{train_i} \cdot D - ZTD_{ERA5P}^{test}}{\left|D - ZTD_{ERA5P}^{train_i}\right| \cdot \left|D - ZTD_{ERA5P}^{test}\right|} \quad (23)$$

where,  $i$  refers to the  $i$ th training station,  $D - ZTD_{ERA5P}^{train_i}$  denotes the vector of the  $i$ th training station in the monthly  $D-ZTD_{ERA5P}$  time series, as well as  $D - ZTD_{ERA5P}^{test}$  for the individual verified station. In order to express more clearly the similarity of the training samples with the verified sample, we give the average-cosine value as

$$\overline{\cos\left(D - ZTD_{ERA5P}^{train_i}, D - ZTD_{ERA5P}^{test}\right)} = \frac{1}{n} \sum_{i=1}^n \cos\left(D - ZTD_{ERA5P}^{train_i}, D - ZTD_{ERA5P}^{test}\right) \quad (24)$$

where  $n$  refers to the number of training stations in each month.

In Figure 12, we divide the available IGS station in January, April, July, and October of 2018 according to the station distribution, the improvement rate  $< 0$ , as well as  $|\text{average cosine}| < 0.2$ . When  $|\text{average cosine}| < 0.2$ , the similarity of the training samples with the verified samples is weak. The overall trend between the average-cosine and the improvement rate tends to be linear from black spots, where the improvement rate increases with the rise of the average-cosine value. The average-cosine values of most stations are more than 0.2 with a positive improvement rate. It implies that the overall accuracy of estimated ZTD from Scheme 3 is superior to the accuracy of ERA5P-ZTD. Moreover, the overall improved accuracy is associated with the similarity between training stations and testing stations.

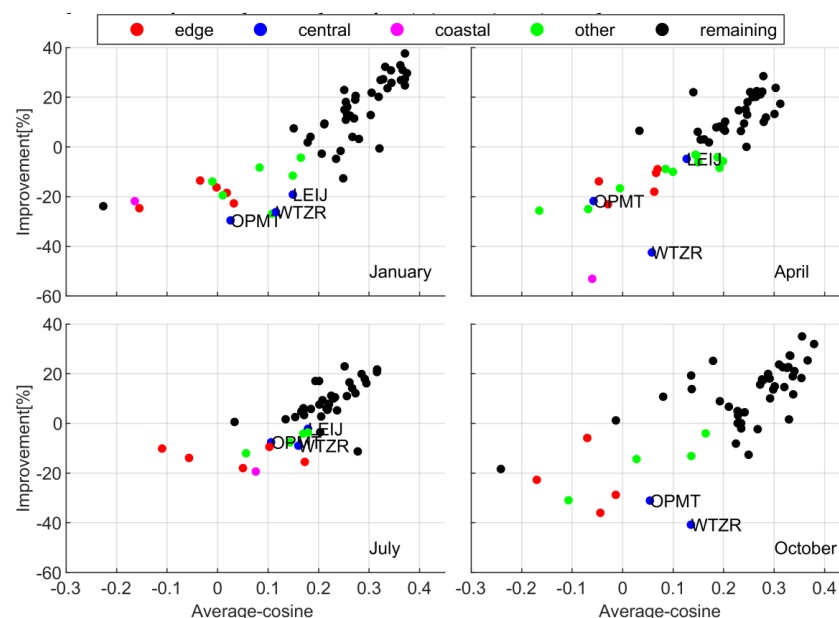


**Figure 12.** Similarity of the improvement rate with average-cosine value for each available station in January, April, July, and October of 2018. Among them, the black spots refer to the station with the improvement rate  $> 0$  or  $|\text{average cosine}| > 0.2$ . The red spots refer to the stations located in the edge region with the improvement rate  $< 0$  and  $|\text{average cosine}| < 0.2$ , the blue spots for the stations located in the central region, and the magenta spots for the stations close to the coast. For the red, blue, and magenta spots, their corresponding stations are included at least three months in January, April, July, and October of 2018. The other stations are presented by using the green spots.

Although the WTZR, OPMT, and LEIJ sites with blue spots are surrounded by a dense network of stations in the central region as shown in Figure 13, their average-cosine values are less than 0.2 at least three months in January, April, July, and October of 2018. The estimated *ZTD* values of the three sites have a negative improvement rate owing to the trained stations have lower similarity with them. For the sites with red, magenta, and green spots, they are always located on the edge of the region or near the coast. On one hand, their locations are relatively outliers when their *ZTD*s are estimated, which also leads to a lower similarity and negative improvement rate. On the other hand, the large change of air humidity often occurs near the coast, and the accuracy of *ZTD* modeling become unstable owing to the influence of the abundant water vapor and active monsoon climate. Overall, this is a common problem for the *ZTD* modeling. Even though, the improvement rate of estimated *ZTD* is positive for most stations, and the biggest improvement rate from Scheme 3 can reach about 40%.

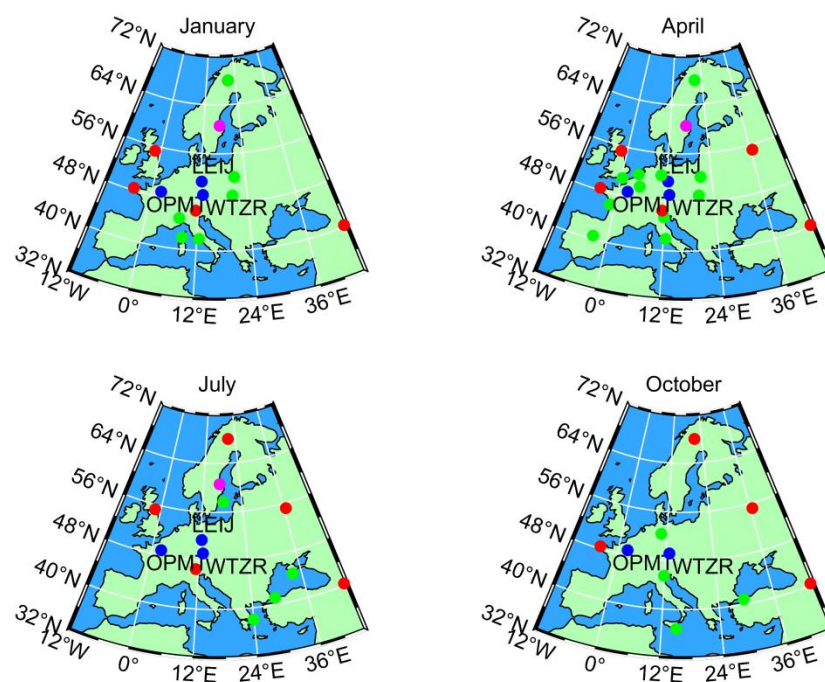


**Figure 13.** Station distribution based on the conditions of improvement rate  $< 0$ , and  $|\text{average cosine}| < 0.2$ . These spots with different color correspond with the colored spots in Figure 12.

## 5. Conclusions

As a fresh meteorological reanalysis data, the *ERA5* data has higher spatial resolution than the *IGS-ZTD*. In addition, the LSSVM algorithm has a more stable computing performance than the traditional BPNN algorithm. In this paper, we combine the *ERA5* data with *IGS-ZTD* by using the LSSVM algorithm. Among them, we extend the *ERA5* data to *ERA5S-ZTD* and *ERA5P-ZTD* based on the model method and integral method, and design three schemes to build *ZTD* models.

The consistency of *ERA5P-ZTD* with *IGS-ZTD* is better than that of *ERA5S-ZTD* owing to the integral method, as well as the multiple pressure-level data. The overall average *RMSE* value is 30.1 mm and 10.7 mm for *ERA5S-ZTD* and *ERA5P-ZTD*, respectively. While they have the same trend with the seasonal variation, the *RMSE* values reach biggest with the coming of summer. In addition, the stations located in low latitudes and coastal regions have always higher *RMSE* values owing to the high heat and active monsoon activities.

For the three *ZTD* models, the overall average monthly bias is 1.1 mm, 0.3 mm, and  $-1.6$  mm, with the corresponding mean value of average *RMSE* values of 25.8 mm, 22.9 mm, and 9.0 mm for Schemes 1, 2, and 3, respectively. Hardly any systematic errors

exist for all three ZTD models based on the LSSVM algorithm, and the ZTD modeling accuracy is significantly improved when the ERA5 data is added, especially for the ZTD model with ERA5P-ZTD. Meanwhile, the seasonal characteristics still exist owing to the accumulation of water vapor and the irregular changes of cyclones in summer, as well as the accuracy limitation of ERA5S-ZTD and ERA5P-ZTD.

To investigate the advantage of the combination of ERA5 data using the LSSVM algorithm, the improvement rates are analyzed and discussed in detail. The overall improvement rate has 19.1% for the ZTD model with ERA5S-ZTD, and 1.6% for the ZTD model with ERA5P-ZTD. The LSSVM algorithm shows excellent performance in correcting systematic and periodic errors of ERA5S-ZTD, while the overall improvement effect is weak for the ZTD model with ERA5P-ZTD.

Moreover, we perform loop verification of each available IGS station to explore the reason for the lower improvement for the ZTD model with ERA5P-ZTD. The dependency of estimated ZTD on the station distribution and the output parameters  $D\text{-ZTD}_{\text{ERA5P}}$  are discussed. On one hand, the improvement rate is positive for most stations located in the central region of the regional network, and the biggest monthly improvement rate can even reach about 40%. On the other hand, the improvement rate is negative for several stations. They are always located on the edge of the region, or near the coast. Additionally, they suffer from both the scarce training samples and more drastic climate variability around them. Furthermore, a few stations are surrounded by a dense network of stations in the central region with a negative improvement rate, which is mainly caused by the lower similarity between the individual verified station and training stations. Overall, the two discussed dependencies are the common problem for the ZTD modeling, and it is important to refine the strategies of multisource combination based on the excellent machine learning algorithms in the near future.

**Author Contributions:** Conceptualization, T.X.; methodology, S.L.; software, S.L.; validation, T.X., N.J. and H.Y.; formal analysis, S.L. and H.Y.; investigation, S.L., S.W. and Z.Z.; resources, T.X.; data curation, S.L.; writing—original draft preparation, S.L.; writing—review and editing, S.L., T.X., N.J. and H.Y.; visualization, S.L. and H.Y.; supervision, T.X. and H.Y.; project administration, T.X.; funding acquisition, T.X. All authors have read and agreed to the published version of the manuscript.

**Funding:** This study is financially supported by the National Key Research & Development Program of China (2020YFB0505800, and 2020YFB0505804), the National Natural Science Foundation of China (41874032) and Natural Science Foundation of Shandong Province, China (ZR2020QD046 and ZR2020MD045).

**Institutional Review Board Statement:** Not applicable.

**Informed Consent Statement:** Informed consent was obtained from all subjects involved in the study.

**Data Availability Statement:** Not applicable.

**Acknowledgments:** The authors would like to extend their sincere gratitude to ECMWF and IGS for providing the relevant data.

**Conflicts of Interest:** The authors declare no conflict of interest.

## References

1. Rocken, C.; Ware, R.; Van Hove, T.; Solheim, F.; Alber, C.; Johnson, J.; Bevis, M.; Businger, S. Sensing atmospheric water vapor with the global positioning system. *Geophys. Res. Lett.* **1993**, *20*, 2631–2634. [[CrossRef](#)]
2. Bevis, M.; Businger, S.; Chiswell, S.; Herring, T.A.; Anthes, R.A.; Rocken, C.; Ware, R.H. GPS Meteorology: Mapping Zenith Wet Delays onto Precipitable Water. *J. Appl. Meteorol.* **1994**, *33*, 379–386. [[CrossRef](#)]
3. Davis, J.L.; Herring, T.A.; Shapiro, I.I.; Rogers, A.E.E.; Elgered, G. Geodesy by radio interferometry: Effects of atmospheric modeling errors on estimates of baseline length. *Radio Sci.* **1985**, *20*, 1593–1607. [[CrossRef](#)]
4. Askne, J.; Nordius, H. estimation of tropospheric delay for microwaves from surface weather data. *Radio Sci.* **1987**, *22*, 379–386. [[CrossRef](#)]
5. Saastamoinen, J. Atmospheric Correction for the Troposphere and Stratosphere in Radio Ranging Satellites. In *Use of Artificial Satellites for Geodesy*; Wiley: Hoboken, NJ, USA, 1972; Volume 15, pp. 247–251.

6. Hopfield, H.S. Two-quartic tropospheric refractivity profile for correcting satellite data. *J. Geophys. Res.* **1969**, *74*, 4487–4499. [[CrossRef](#)]
7. Collins, J.P.; Langley, R.B. The residual tropospheric propagation delay: How bad can it get? In Proceedings of the Proc. ON GPS 1998, 11th International Technical Meeting of the Satellite Division of the Institute of Navigation, Nashville, TN, USA, 15–18 September 1998; pp. 729–738.
8. Penna, N.; Dodson, A.; Chen, W. Assessment of EGNOS tropospheric correction model. *J. Navig.* **2001**, *54*, 37–55. [[CrossRef](#)]
9. Boehm, J.; Heinkelmann, R.; Schuh, H. Short Note: A global model of pressure and temperature for geodetic applications. *J. Geod.* **2007**, *81*, 679–683. [[CrossRef](#)]
10. Lagler, K.; Schindelegger, M.; Bohm, J.; Krasna, H.; Nilsson, T. GPT2: Empirical slant delay model for radio space geodetic techniques. *Geophys. Res. Lett.* **2013**, *40*, 1069–1073. [[CrossRef](#)] [[PubMed](#)]
11. Landskron, D.; Bohm, J. VMF3/GPT3: Refined discrete and empirical troposphere mapping functions. *J. Geod.* **2018**, *92*, 349–360. [[CrossRef](#)]
12. Wang, S.; Xu, T.; Nie, W.; Jiang, C.; Yang, Y.; Fang, Z.; Li, M.; Zhang, Z. Evaluation of Precipitable Water Vapor from Five Reanalysis Products with Ground-Based GNSS Observations. *Remote Sens.* **2020**, *12*, 1817. [[CrossRef](#)]
13. Ding, M. A neural network model for predicting weighted mean temperature. *J. Geod.* **2018**, *92*, 1187–1198. [[CrossRef](#)]
14. Ding, M. A second generation of the neural network model for predicting weighted mean temperature. *GPS Solut.* **2020**, *24*, 61. [[CrossRef](#)]
15. Benevides, P.; Catalao, J.; Nico, G. Neural Network Approach to Forecast Hourly Intense Rainfall Using GNSS Precipitable Water Vapor and Meteorological Sensors. *Remote Sens.* **2019**, *11*, 966. [[CrossRef](#)]
16. Pan, Y.; Ren, C.; Liang, Y.; Zhang, Z.; Shi, Y. Inversion of surface vegetation water content based on GNSS-IR and MODIS data fusion. *Satell. Navig.* **2020**, *1*. [[CrossRef](#)]
17. Katsougiannopoulos, S.; Pikridas, C. Prediction of zenith tropospheric delay by multi-layer perceptron. *J. Appl. Geod.* **2009**, *3*, 223–229. [[CrossRef](#)]
18. Suparta, W.; Alhasa, K.M. Application of ANFIS Model for Prediction of Zenith Tropospheric Delay. In Proceedings of the 2013 3rd International Conference on Instrumentation, Communications, Information Technology, and Biomedical Engineering (ICICI-BME), Bandung, Indonesia, 7–8 November 2013; pp. 172–177.
19. Suparta, W.; Alhasa, K.M. *Modeling of Tropospheric Delays Using ANFIS*; Springer: Berlin/Heidelberg, Germany, 2016. [[CrossRef](#)]
20. Xiao, G.W.; Ou, J.K.; Liu, G.L.; Zhang, H.X. Construction of a regional precise tropospheric delay model based on improved BP neural network. *Chin. J. Geophys. Chin. Ed.* **2018**, *61*, 3139–3148. [[CrossRef](#)]
21. Zhang, Q.; Li, F.; Zhang, S.; Li, W. Modeling and Forecasting the GPS Zenith Troposphere Delay in West Antarctica Based on Different Blind Source Separation Methods and Deep Learning. *Sensors* **2020**, *20*, 2343. [[CrossRef](#)] [[PubMed](#)]
22. Albergel, C.; Dutra, E.; Munier, S.; Calvet, J.-C.; Munoz-Sabater, J.; de Rosnay, P.; Balsamo, G. ERA-5 and ERA-Interim driven ISBA land surface model simulations: Which one performs better? *Hydrol. Earth Syst. Sci.* **2018**, *22*, 3515–3532. [[CrossRef](#)]
23. Sun, Z.; Zhang, B.; Yao, Y. An ERA5-Based Model for Estimating Tropospheric Delay and Weighted Mean Temperature Over China With Improved Spatiotemporal Resolutions. *Earth Space Sci.* **2019**, *6*, 1926–1941. [[CrossRef](#)]
24. Jiang, C.; Xu, T.; Wang, S.; Nie, W.; Sun, Z. Evaluation of Zenith Tropospheric Delay Derived from ERA5 Data over China Using GNSS Observations. *Remote Sens.* **2020**, *12*, 663. [[CrossRef](#)]
25. Pavlis, N.K.; Holmes, S.A.; Kenyon, S.C.; Factor, J.K. The development and evaluation of the Earth Gravitational Model 2008 (EGM2008). *J. Geophys. Res. Solid Earth* **2012**, *117*. [[CrossRef](#)]
26. Suykens, J.A.K.; Vandewalle, J. Least squares support vector machine classifiers. *Neural Process. Lett.* **1999**, *9*, 293–300. [[CrossRef](#)]
27. Li, R.; Zheng, S.; Wang, E.; Chen, J.; Feng, S.; Wang, D.; Dai, L. Advances in BeiDou Navigation Satellite System (BDS) and satellite navigation augmentation technologies. *Satell. Navig.* **2020**, *1*. [[CrossRef](#)]
28. Kima, M.-C.; Choi, K.-S. A comparison of collocation-based similarity measures in query expansion. *Inf. Process. Manag.* **1999**, *35*, 19–30. [[CrossRef](#)]